Authors
Jiachen Ding, Ping Yang, Robert E Holz, Steven Platnick, Kerry G Meyer, Mark A Vaughan, Yongxiang Hu, and Michael D King

This article is available at CU Scholar: https://scholar.colorado.edu/lasp_facpapers/4

Ice cloud backscatter study and comparison with CALIPSO and MODIS satellite data

Jiachen Ding,[1] Ping Yang,[1,*] Robert E. Holz,[2] Steven Platnick,[3] Kerry G. Meyer,[3,4] Mark A. Vaughan,[5] Yongxiang Hu,[5] and Michael D. King[6]

[1]*Department of Atmospheric Sciences, Texas A&M University, College Station, TX, USA*
[2]*Space Science and Engineering Center, University of Wisconsin, Madison, WI, USA*
[3]*NASA Goddard Space Flight Center, Greenbelt, MD, USA*
[4]*Goddard Earth Sciences Technology and Research, Universities Space Research Association, Columbia, MD, USA*
[5]*NASA Langley Research Center, Hampton, VA, USA*
[6]*Laboratory for Atmospheric & Space Physics, University of Colorado, CO, USA*
[*]*pyang@tamu.edu*

Abstract: An invariant imbedding T-matrix (II-TM) method is used to calculate the single-scattering properties of 8-column aggregate ice crystals. The II-TM based backscatter values are compared with those calculated by the improved geometric-optics method (IGOM) to refine the backscattering properties of the ice cloud radiative model used in the MODIS Collection 6 cloud optical property product. The integrated attenuated backscatter-to-cloud optical depth (IAB-ICOD) relation is derived from simulations using a CALIPSO (Cloud-Aerosol Lidar and Infrared Pathfinder Satellite) lidar simulator based on a Monte Carlo radiative transfer model. By comparing the simulation results and co-located CALIPSO and MODIS (Moderate Resolution Imaging Spectroradiometer) observations, the non-uniform zonal distribution of ice clouds over ocean is characterized in terms of a mixture of smooth and rough ice particles. The percentage of the smooth particles is approximately 6% and 9% for tropical and midlatitude ice clouds, respectively.

©2015 Optical Society of America

OCIS codes: (000.0000) General; (000.2700) General science.

References

1. K. N. Liou, "Influence of cirrus clouds on weather and climate processes: A global perspective," Mon. Weather Rev. **114**(6), 1167–1199 (1986).
2. G. L. Stephens, S. C. Tsay, P. W. Stackhouse, Jr., and P. J. Flatau, "The relevance of the microphysical and radiative properties of cirrus clouds to climate and climatic feedback," J. Atmos. Sci. **47**(14), 1742–1754 (1990).
3. M. D. Zelinka, S. A. Klein, and D. L. Hartmann, "Computing and partitioning cloud feedbacks using cloud property histograms. Part I: Cloud radiative kernels," J. Clim. **25**(11), 3715–3735 (2012).
4. C. Zhou, A. E. Dessler, M. D. Zelinka, P. Yang, and T. Wang, "Cirrus feedback on interannual climate fluctuations," Geophys. Res. Lett. **41**(24), 9166–9173 (2014).
5. C. M. R. Platt, "Lidar and radiometric observations of cirrus clouds," J. Atmos. Sci. **30**(6), 1191–1204 (1973).
6. C. M. R. Platt, "Remote sounding of high clouds: I. Calculation of visible and infrared optical properties from lidar and radiometer measurements," J. Appl. Meteorol. **18**(9), 1130–1143 (1979).
7. C. M. R. Platt, D. W. Reynolds, and N. L. Abshire, "Satellite and lidar observations of the albedo, emittance and optical depth of cirrus compared to model calculations," Mon. Weather Rev. **108**(2), 195–204 (1980).
8. C. M. R. Platt, "Remote sounding of high clouds. III: Monte Carlo calculations of multiple-scattered lidar returns," J. Atmos. Sci. **38**(1), 156–167 (1981).
9. Z. Wang and K. Sassen, "Cirrus cloud microphysical property retrieval using lidar and radar measurements. Part I: Algorithm description and comparison with in situ data," J. Appl. Meteorol. **41**(3), 218–229 (2002).
10. Z. Wang and K. Sassen, "Cirrus cloud microphysical property retrieval using lidar and radar measurements. Part II: Midlatitude cirrus microphysical and radiative properties," J. Atmos. Sci. **59**(14), 2291–2302 (2002).
11. D. M. Winker, J. Pelon, J. A. Coakley, Jr., S. A. Ackerman, R. J. Charlson, P. R. Colarco, P. Flamant, Q. Fu, R. Hoff, C. Kittaka, T. L. Kubar, H. Le Treut, M. P. McCormick, G. Megie, L. Poole, K. Powell, C. Trepte, M. A. Vaughan, and B. A. Wielicki, "The CALIPSO Mission: A Global 3D View Of Aerosols And Clouds," Bull. Am. Meteorol. Soc. **91**(9), 1211–1229 (2010).

#253394 Received 5 Nov 2015; revised 21 Dec 2015; accepted 4 Jan 2016; published 8 Jan 2016
© 2016 OSA

12. M. Hayman, S. Spuler, B. Morley, and J. VanAndel, "Polarization lidar operation for measuring backscatter phase matrices of oriented scatterers," Opt. Express **20**(28), 29553–29567 (2012).
13. H. Okamoto, K. Sato, and Y. Hagihara, "Global analysis of ice microphysics from CloudSat and CALIPSO: Incorporation of specular reflection in lidar signals," J. Geophys. Res. **115**(D22), D22209 (2010).
14. D. Josset, J. Pelon, A. Garnier, Y. Hu, M. Vaughan, P. W. Zhai, R. Kuehn, and P. Lucker, "Cirrus optical depth and lidar ratio retrieval from combined CALIPSO-CloudSat observations using ocean surface echo," J. Geophys. Res. **117**(D5), D05207 (2012).
15. M. Reverdy, V. Noel, H. Chepfer, and B. Legras, "On the origin of subvisible cirrus clouds in the tropical upper troposphere," Atmos. Chem. Phys. **12**(24), 12081–12101 (2012).
16. A. Ansmann, M. Riebesell, U. Wandinger, C. Weitkamp, E. Voss, W. Lahmann, and W. Michaelis, "Combined Raman elastic-backscatter lidar for vertical profiling of moisture, aerosol extinction, backscatter, and lidar ratio," Appl. Phys. B **55**(1), 18–28 (1992).
17. W. N. Chen, C. W. Chiang, and J. B. Nee, "Lidar ratio and depolarization ratio for cirrus clouds," Appl. Opt. **41**(30), 6470–6476 (2002).
18. T. Sakai, T. Nagai, M. Nakazato, Y. Mano, and T. Matsumura, "Ice clouds and Asian dust studied with lidar measurements of particle extinction-to-backscatter ratio, particle depolarization, and water-vapor mixing ratio over Tsukuba," Appl. Opt. **42**(36), 7103–7116 (2003).
19. V. Noel, D. M. Winker, T. J. Garrett, and M. Mcgill, "Extinction coefficients retrieved in deep tropical ice clouds from lidar observations using a CALIPSO-like algorithm compared to in-situ measurements from the cloud integrating nephelometer during CRYSTAL-FACE," Atmos. Chem. Phys. **7**(5), 1415–1422 (2007).
20. M. Oo and R. Holz, "Improving the CALIOP aerosol optical depth using combined MODIS-CALIOP observations and CALIOP integrated attenuated total color ratio," J. Geophys. Res. **116**(D14), D14201 (2011).
21. D. M. Winker, "Accounting for multiple scattering in retrievals from space lidar," Proc. SPIE **5059**, 128 (2003).
22. K. N. Liou and Y. Takano, "Light scattering by nonspherical particles: remote sensing and climatic implications," Atmos. Res. **31**(4), 271–298 (1994).
23. P. Yang and K. N. Liou, "Light scattering and absorption by nonspherical ice crystals," in *Light Scattering Reviews: Single and Multiple Light Scattering,* Ed. A. Kokhanovsky, Springer-Praxis Publishing, Chichester, UK, 31–71 (2006).
24. A. J. Baran, "From the single-scattering properties of ice crystals to climate prediction: A way forward," Atmos. Res. **112**, 45–69 (2012).
25. P. Yang, K. N. Liou, L. Bi, C. Liu, B. Q. Yi, and B. A. Baum, "On the radiative properties of ice clouds: Light scattering, remote sensing, and radiation parameterization," Adv. Atmos. Sci. **32**(1), 32–63 (2015).
26. J. Um and G. M. McFarquhar, "Single-scattering properties of aggregates of plates," Q. J. R. Meteorol. Soc. **135**(639), 291–304 (2009).
27. J. Um and G. M. McFarquhar, "Optimal numerical methods for determining the orientation averages of single-scattering properties of atmospheric ice crystals," J. Quant. Spectrosc. Radiat. Transf. **127**, 207–223 (2013).
28. J. Um and G. M. McFarquhar, "Single-scattering properties of aggregates of bullet rosettes in cirrus," J. Appl. Meteorol. Climatol. **46**(6), 757–775 (2007).
29. B. R. Johnson, "Invariant imbedding T matrix approach to electromagnetic scattering," Appl. Opt. **27**(23), 4861–4873 (1988).
30. L. Bi and P. Yang, "Accurate simulation of the optical properties of atmospheric ice crystals with the invariant imbedding T-matrix method," J. Quant. Spectrosc. Radiat. Transf. **138**, 17–35 (2014).
31. P. Yang and K. N. Liou, "Geometric-optics-integral-equation method for light scattering by nonspherical ice crystals," Appl. Opt. **35**(33), 6568–6584 (1996).
32. C. Zhou and P. Yang, "Backscattering peak of ice cloud particles," Opt. Express **23**(9), 11995–12003 (2015).
33. Y. Hu, D. Winker, P. Yang, B. A. Baum, L. Poole, and L. Vann, "Identification of cloud phase from PICASSO-CENA lidar depolarization: A multiple scattering sensitivity study," J. Quant. Spectrosc. Radiat. Transf. **70**(4-6), 569–579 (2001).
34. C. R. Parkinson, "Aqua: An Earth-observing satellite mission to examine water and other climate variables," IEEE Trans. Geosci. Rem. Sens. **41**(2), 173–183 (2003).
35. T. S. L'Ecuyer and J. H. Jiang, "Touring the atmosphere aboard the A-Train," Phys. Today **63**(7), 36–41 (2010).
36. G. L. Stephens, D. G. Vane, R. J. Boain, G. G. Mace, K. Sassen, Z. Wang, A. J. Illingworth, E. J. O'Connor, W. B. Rossow, S. L. Durden, S. D. Miller, R. T. Austin, A. Benedetti, C. Mitrescu, and The CloudSat Science Team, "The CloudSat mission and the A-Train: A new dimension of space-based observations of clouds and precipitation," Bull. Am. Meteorol. Soc. **83**(12), 1771–1790 (2002).
37. M. D. King, W. P. Menzel, Y. J. Kaufman, D. Tanré, B. C. Gao, S. Platnick, S. A. Ackerman, L. A. Remer, R. Pincus, and P. A. Hubanks, "Cloud and aerosol properties, precipitable water, and profiles of temperature and water vapor from MODIS," IEEE Trans. Geosci. Rem. Sens. **41**(2), 442–458 (2003).
38. D. M. Winker, M. A. Vaughan, A. Omar, Y. Hu, K. A. Powell, Z. Liu, W. H. Hunt, and S. A. Young, "Overview of the CALIPSO mission and CALIOP data processing algorithms," J. Atmos. Ocean. Technol. **26**(11), 2310–2323 (2009).
39. D. M. Winker and L. R. Poole, "Monte-Carlo calculations of cloud returns for ground-based and space-based lidars," Appl. Phys. B **60**(4), 341–344 (1995).
40. W. J. Wiscombe, "The delta-M method: rapid yet accurate radiative flux calculations for strongly asymmetric phase functions," J. Atmos. Sci. **34**(9), 1408–1422 (1977).

#253394 Received 5 Nov 2015; revised 21 Dec 2015; accepted 4 Jan 2016; published 8 Jan 2016
© 2016 OSA

41. K. N. Liou, *An introduction to atmospheric radiation* (Academic, 2002).
42. M. Wendisch and P. Yang, *Theory of atmospheric radiative transfer* (John Wiley & Sons, 2012).
43. W. H. Hunt, D. M. Winker, M. A. Vaughan, K. A. Powell, P. L. Lucker, and C. Weimer, "CALIPSO Lidar Description and Performance Assessment," J. Atmos. Ocean. Technol. **26**(7), 1214–1228 (2009).
44. J. W. Hovenier and C. V. M. Van der Mee, "Fundamental relationships relevant to the transfer of polarized light in a scattering atmosphere," Astron. Astrophys. **128**, 1–16 (1983).
45. P. Yang, L. Bi, B. A. Baum, K. N. Liou, G. W. Kattawar, M. I. Mishchenko, and B. Cole, "Spectrally consistent scattering, absorption, and polarization properties of atmospheric ice crystals at wavelengths from 0.2 to 100 μ m," J. Atmos. Sci. **70**(1), 330–347 (2013).
46. B. A. Baum, A. J. Heymsfield, P. Yang, and S. T. Bedka, "Bulk scattering properties for the remote sensing of ice clouds. Part I: Microphysical data and models," J. Appl. Meteorol. **44**(12), 1885–1895 (2005).
47. B. A. Baum, P. Yang, A. J. Heymsfield, S. Platnick, M. D. King, Y. Hu, and S. T. Bedka, "Bulk scattering properties for the remote sensing of ice clouds. Part II: Narrowband models," J. Appl. Meteorol. **44**(12), 1896–1911 (2005).
48. R. E. Holz, S. Platnick, K. Meyer, M. Vaughan, A. Heidinger, P. Yang, G. Wind, S. Dutcher, S. Ackerman, N. Amarasinghe, F. Nagle, and C. Wang, "Resolving cirrus optical thickness biases between CALIOP and MODIS using infrared retrievals," Atmos. Chem. Phys. Discuss. **15**(20), 29455–29495 (2015).
49. B. A. Baum, P. Yang, A. J. Heymsfield, A. Bansemer, B. H. Cole, A. Merrelli, C. Schmitt, and C. Wang, "Ice cloud single-scattering property models with the full phase matrix at wavelengths from 0.2 to 100μm," J. Quant. Spectrosc. Radiat. Transf. **146**, 123–139 (2014).
50. P. Yang, G. W. Kattawar, G. Hong, P. Minnis, and Y. Hu, "Uncertainties associated with the surface texture of ice particles in satellite-based retrieval of cirrus clouds—Part I: Single-scattering properties of ice crystals with surface roughness," IEEE Trans. Geosci. Rem. Sens. **46**(7), 1940–1947 (2008).
51. B. Yi, P. Yang, B. A. Baum, T. L'Ecuyer, L. Oreopoulos, E. J. Mlawer, A. J. Heymsfield, and K. N. Liou, "Influence of ice particle surface roughening on the global cloud radiative effect," J. Atmos. Sci. **70**(9), 2794–2807 (2013).
52. B. H. Cole, P. Yang, B. A. Baum, J. Riedi, and L. C. Labonnote, "Ice particle habit and surface roughness derived from PARASOL polarization measurements," Atmos. Chem. Phys. **14**(7), 3739–3750 (2014).
53. S. Iwasaki and H. Okamoto, "Analysis of the enhancement of backscattering by nonspherical particles with flat surfaces," Appl. Opt. **40**(33), 6121–6129 (2001).
54. A. Borovoi, A. Konoshonkin, and N. Kustova, "Backscattering by hexagonal ice crystals of cirrus clouds," Opt. Lett. **38**(15), 2881–2884 (2013).
55. A. G. Borovoi and N. V. Kustova, "Light scattering by large faceted particles," in *Polarimetric Detection, Characterization and Remote Sensing*, M. I. Mishchenko, Y. S. Yatskiv, V. K. Rosenbush, and G. Videen, eds. (NATO Science for Peace and Security 2011).
56. A. G. Borovoi and I. A. Grishin, "Scattering matrices for large ice crystal particles," J. Opt. Soc. Am. A **20**(11), 2071–2080 (2003).
57. A. Garnier, J. Pelon, M. A. Vaughan, D. M. Winker, C. R. Trepte, and P. Dubuisson, "Lidar multiple scattering factors inferred from CALIPSO lidar and IIR retrievals of semi-transparent cirrus cloud optical depths over oceans," Atmos. Meas. Tech. **8**(7), 2759–2774 (2015).
58. G. B. Arfken and H. J. Weber, *Mathematical Methods For Physicists*, (6th Edition, Elsevier Academic Press, 2005).
59. S. Platnick, S. Ackerman, M. King, *MODIS Atmosphere L2 Cloud Product (06_L2). NASA MODIS Adaptive Processing System*, (Goddard Space Flight Center, 2015).
60. H. J. aufm Kampe, H. K. Weickmann, and J. J. Kelly, "The influence of temperature on the shape of ice crystals growing at water saturation," J. Meteorol. **8**(3), 168–174 (1951).
61. A. J. Heymsfield and C. M. R. Platt, "A Parameterization of the Particle Size Spectrum of Ice Clouds in Terms of the Ambient Temperature and the Ice Water Content," J. Atmos. Sci. **41**(5), 846–855 (1984).
62. J. Hallett and B. J. Mason, "The influence of temperature and supersaturation on the habit of ice crystals grown from the vapour," in *Proceedings of the Royal Society of London A: Mathematical, Physical and Engineering Sciences* (The Royal Society, 1958), pp. 440–453.

1. Introduction

Ice clouds play a significant role in the Earth's radiation budget and climate [1–4]. The cooling or warming effect of an ice cloud depends on the microphysical properties of the cloud (e.g., ice crystal shape and size) and the relevant optical properties such as ice cloud optical depth (ICOD). However, accurately measuring ice cloud properties and their variations on a global scale is quite challenging.

Satellite remote sensing observations are widely used to infer ice cloud properties. Specifically, active lidar observations provide useful information for retrieving the microphysical and optical properties of ice clouds [5–13]. For cloudy scenes, lidar signals are mainly determined by the bulk backscattering properties of cloud particles. A critical lidar

#253394 Received 5 Nov 2015; revised 21 Dec 2015; accepted 4 Jan 2016; published 8 Jan 2016
© 2016 OSA

measurement is the integrated attenuated backscatter (IAB), which is an integration of the backscattered light after attenuation through a cloud layer [5]. IAB is largely related to optical depth [5]; thus, the optical depth of a cloud or aerosol layer can be derived directly from IAB measurements [14,15] if the relevant optical depth is smaller than approximately 3. However, two additional parameters are required, namely, the lidar ratio (LR) and the multiple scattering coefficient (MSC). The lidar ratio is physically defined as the ratio of the volume extinction coefficient to the volume backscatter coefficient, and is proportional to the inverse of the phase function in the 180° backscattering direction. The LR of ice clouds is therefore a function of the backscattering properties of the clouds, and, under certain conditions such as high signal to noise, can be inferred directly from lidar measurements [16–18]. By assuming appropriate LRs, measured backscatter can help determine cloud extinction, the vertical integral of which is optical depth [19,20]. The MSC, a correction factor that accounts for the multiple scattering of photons within the cloud that are subsequently detected by the lidar receiver, depends on the receiver design and distance from the target; and it is a pre-specified parameter in ICOD retrievals using lidar IAB, and therefore an additional source of ICOD retrieval uncertainty [21].

The microphysical and optical properties of ice clouds have been extensively studied [22–25]. The single scattering properties of distinct ice crystal habits (shapes) [26–28] with various microphysical characteristics such as surface roughness and internal inhomogeneity can be calculated using numerical approaches. Currently, numerically rigorous methods such as the invariant imbedding T-matrix method (II-TM) [29,30] can only calculate the single-scattering properties of particles that are much smaller than the typical ice crystals found within ice clouds at lidar application wavelengths (e.g. 532nm) due to computational resource limitation. Only geometric optics methods such as the improved geometric optics method (IGOM) [31] are applicable for larger particles. Geometric optics methods are accurate enough for large particles except for backscatter computations [32].

In this study, the scattering properties of ice crystals are calculated using both the II-TM and IGOM. Synergically combining the results from the two methods, a refined ice cloud radiative property model for the backscatter direction is suggested. We then simulate the IAB-ICOD relation for several ice cloud radiative property models using a Monte Carlo radiative transfer model (MCRTM), which is a modified version of that developed by Hu et al. [33]. The simulation results are compared with observations from the Moderate Resolution Imaging Spectroradiometer (MODIS) onboard the Aqua satellite [34] and the Cloud-Aerosol Lidar with Orthogonal Polarization (CALIOP) on the Cloud-Aerosol Lidar and Infrared Pathfinder Satellite (CALIPSO) platform [11]. Both satellites fly in the A-train constellation [35] and view the same location less than 3 minutes apart [36], and thus in most cases measure the properties of the same clouds. MODIS level 2 data provides retrieved optical depths of ice clouds [37] and CALIPSO level 2 lidar data [38] provides measured integrated attenuated backscatter values associated with ice clouds. By co-locating the two data sets, the retrieved IAB-ICOD relation can be compared with the simulation.

The remainder of this paper is organized as follows: Section 2 describes the theory, methodology, and data used in the study. Section 3 presents, compares, and analyzes the simulation results of the IAB-ICOD relation and satellite data. Section 4 gives a summary and conclusions.

2. Theory and methodology

2.1. Integrated attenuated backscatter-cloud optical depth relation

The IAB-ICOD relation is defined in terms of ice cloud optical depth (τ) by [5,14]

$$\tau = -\frac{1}{2\eta}\ln\left(1-2\eta S\gamma'\right) \tag{1}$$

#253394 Received 5 Nov 2015; revised 21 Dec 2015; accepted 4 Jan 2016; published 8 Jan 2016
© 2016 OSA

or in terms of IAB (γ') by

$$\gamma' = \frac{1}{2\eta S}\left(1 - e^{-2\eta\tau}\right) \tag{2}$$

where S is the lidar ratio and η is the multiple scattering coefficient. The detailed derivation of the above relation is discussed in [5], where η is implicitly assumed to be independent of optical depth for a uniform number concentration distribution of particles in clouds. The lidar ratio, in units of *sr* is the ratio of the volume extinction coefficient to the volume backscatter coefficient and can be given in terms of the backscattering phase function value in the form:

$$S = \frac{4\pi}{P_{11}(180^\circ)\tilde{\omega}} \tag{3}$$

where $P_{11}(180^\circ)$ is the phase function in the 180° backscattering direction and $\tilde{\omega}$ is the single-scattering albedo (SSA). For a non-absorbing particle, i.e., $\tilde{\omega}$ = 1, S is then simply the inverse of the normalized phase function at scattering angle 180° [14]. The multiple scattering coefficient η is the ratio of apparent experimental visible extinction coefficient to true visible extinction coefficient, and has the interval (0, 1] with $\eta = 1$ indicating no multiple scattering.

From Eq. (2), it is obvious that the IAB approaches the constant $1/2\eta S$ when optical depth is extremely large. This suggests that there is a critical value of IAB for each cloud, and that lidars can only detect far boundaries of layers with relatively small optical depth, typically τ less than approximately 3 to 4.

2.2. CALIOP lidar simulation

A simulator based on a Monte Carlo radiative transfer model (MCRTM) is used to simulate the signals received by the CALIOP lidar. MCRTM is similar to a ray-tracing method; thus by tracing the random paths of a large number of photons, the distribution of scattered light can be quantified if there are sufficient photons to lead to a convergence of the simulations. MCRTM can directly model almost any physical scattering process [39], though it is computationally expensive.

In the original model by Hu et al. [33], the bulk phase function of cloud particles is directly used in the simulation. For an ice crystal of typical size, the forward direction of the phase function at a non-absorbing wavelength is always sharply peaked, which can result in errors when determining the scattering angle. In the modified version used here, the Delta-M Method (DMM) [40] is applied to truncate the forward scattering peak of the phase function. Note that after truncation, the SSA, optical depth, and other output results must be scaled based on the similarity principle [40–42].

For the CALIOP lidar, the field of view (FOV) of the receiver is 130 μrad, the satellite altitude (H_s) is 705km above mean sea level, and the pointing angle (θ_0) is 3° from nadir [43] with azimuth assumed to be zero. The laser transmits linearly polarized light at 1064 nm and 532 nm, with the backscatter at 1064 nm being measured by a single avalanche photodiode. At 532 nm, a polarization beam splitter and a pair of photomultiplier tubes are used to separately measure the backscattered light polarized both parallel and perpendicular to the polarization plane of the transmitted beam [43]. Simulation inputs include the number of cloud layers, along with the cloud top (H_{ti}) and base (H_{bi}) altitudes (i is the index of cloud layers from top to bottom), cloud optical depths (τ_i), and the scattering properties for each cloud layer. Each single layer is divided into some number of bins similar to the range bins in a lidar signal and the numbers of bins can be specified in the simulator. The mean cloud

#253394 Received 5 Nov 2015; revised 21 Dec 2015; accepted 4 Jan 2016; published 8 Jan 2016
© 2016 OSA

extinction coefficient is $\beta_i = \tau_i / (H_{ti} - H_{bi})$. In addition, a sufficient number of photons are specified such that the results converge.

Each new "incident" photon is initialized before tracing. The initial location of the photon is on the top of the highest layer ($z = 0$, $\tau = 0$, the positive z direction is downward), with the horizontal location defined as $x = (H_s - H_{t0}) \tan\theta_0$, $y = 0$. The initial photon direction is $\theta = \theta_0$, with azimuth angle $\varphi = 0$. The initial Stokes vector of the photon is $(I_0, Q_0, U_0, V_0)^T$, where $U_0 = V_0 = 0$. Two separated channels receive two orthogonally polarized backscatter components respectively at 532 nm while the backscatter at 1064 nm is received by only one channel. Thus, $I_0 = Q_0 = 1$ at 532 nm and $I_0 = 1$, $Q_0 = 0$ at 1064 nm in the simulations.

Photon tracing simulates the location of each photon-particle interaction. The interaction occurs at optical depth

$$\Delta\tau = -\mu_0 \ln r_1 \tag{4}$$

where $\mu_0 = \cos\theta_0$ and r_1 is a uniform random number ranging from 0 to 1. Thus, the normal location of the photon is $\tau = \tau + \Delta\tau$, $z = z + \Delta z$. If $\tau < \tau_0$, the interaction occurs in the first cloud layer, and

$$\Delta z = \Delta\tau / \beta_0 \tag{5}$$

If $\tau_0 + \cdots + \tau_{i-1} < \tau < \tau_0 + \cdots + \tau_{i-1} + \tau_i$, the photon is scattered or absorbed in the *ith* layer, and

$$\Delta z = \sum_{j=0}^{i-1} \frac{\tau_j}{\beta_j} + \frac{\tau - \sum_{j=0}^{i-1} \tau_j}{\beta_i} \tag{6}$$

The photon's horizontal location, regardless of interaction layer, is $x = x + \Delta z \tan\theta \cos\varphi$ and $y = y + \Delta z \tan\theta \sin\varphi$. If $\tau > \tau_0 + \cdots + \tau_l$, where τ_l is the lowest cloud layer, the photon exits the cloud and no energy is reflected back to the sensor. The configuration of the atmosphere in the simulation is shown in Fig. 1. The detailed steps of photon tracing procedure are explained in [33].

#253394 Received 5 Nov 2015; revised 21 Dec 2015; accepted 4 Jan 2016; published 8 Jan 2016
© 2016 OSA

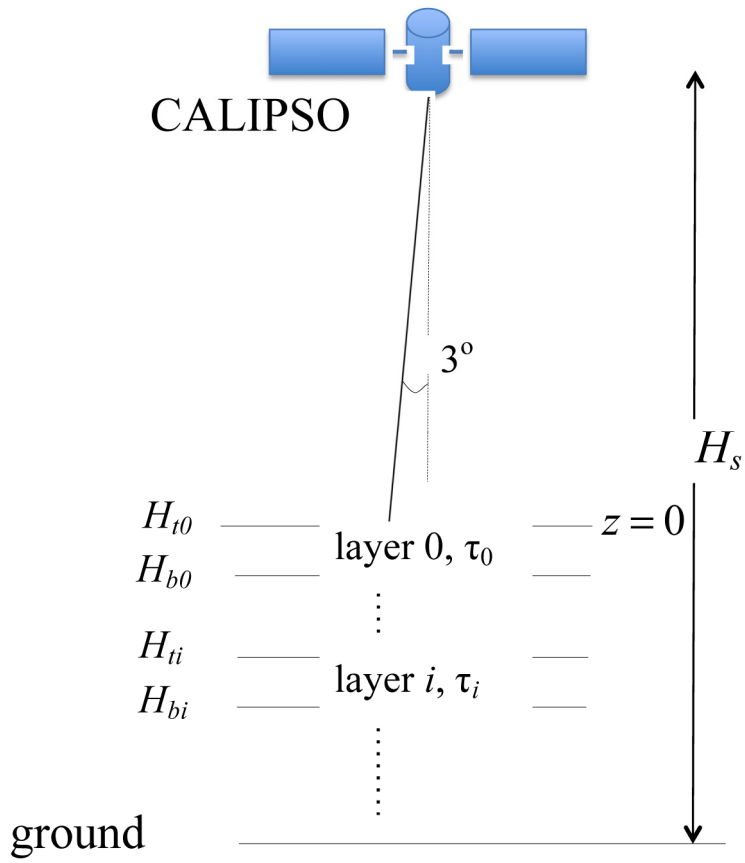

Fig. 1. Configuration of the atmosphere in the CALIPSO lidar simulator.

If the photon remains in the clouds and is not beyond the maximum receivable range $R_{\max} = (H_s - H_{t0} + \Delta z)\tan(FOV/2)$, the portion of energy reflected back to the sensor is

$$\begin{pmatrix} I \\ Q \\ U \\ V \end{pmatrix} = \tilde{\omega}\Delta\Omega_{re}\exp(-\frac{\tau}{\cos\theta_r})L(\varphi_r)L(\pi-\varphi_2)P(\Theta)L(-\varphi_1)\begin{pmatrix} I_0 \\ Q_0 \\ U_0 \\ V_0 \end{pmatrix} \tag{7}$$

where $\Delta\Omega_{re}$ is the lidar receiver's aperture (a solid angle), $P(\Theta)$ is the bulk phase matrix of cloud particles, Θ is the scattering angle, θ_r is the zenith angle of the propagation direction of a photon scattered back to the lidar and φ_r is the angle between the scattering plane and the initial lidar coordinate. L is the rotation matrix and $-\varphi_1$ and $\pi-\varphi_2$ are the angles between the photon's polarization reference plane and the scattering plane before and after scattering, respectively. Θ, φ_1 and φ_2 can be analytically calculated according to spherical trigonometry relations [33,44]. The rotation matrix is defined as

#253394 Received 5 Nov 2015; revised 21 Dec 2015; accepted 4 Jan 2016; published 8 Jan 2016
© 2016 OSA

$$L(\varphi)=\begin{pmatrix}1 & 0 & 0 & 0\\ 0 & \cos 2\varphi & \sin 2\varphi & 0\\ 0 & -\sin 2\varphi & \cos 2\varphi & 0\\ 0 & 0 & 0 & 1\end{pmatrix} \tag{8}$$

The scattering direction can then be determined using the phase function and two uniformly distributed random numbers r_2 and r_3, such that

$$r_2=\frac{\int_0^{\mu_s} P_{11}(\mu')d\mu'}{\int_0^1 P_{11}(\mu')d\mu'} \tag{9}$$

$$\Phi=2\pi r_3 \tag{10}$$

where $\mu_s=\cos\Theta$ is the cosine of the zenith component of scattering angle and Φ is the azimuth component. The Stokes vector of the photon after scattering becomes

$$\begin{pmatrix}I'\\ Q'\\ U'\\ V'\end{pmatrix}=\tilde{\omega}L(\pi-\varphi_2)P(\Theta)L(-\varphi_1)\begin{pmatrix}I\\ Q\\ U\\ V\end{pmatrix} \tag{11}$$

If the photon is within the cloud, the location of next the photon-particle interaction is determined by Eq. (4), and Eq. (5) to Eq. (11) are followed to determine the energy scattered back to the receiver from the interaction. The photon is traced following these steps until it exits the cloud or is absorbed. The absorption is expressed by $wt_a=wt_a\times\tilde{\omega}$ where wt_a indicates the energy proportion of the traced photon. If wt_a is less than a very small number (i.e. 1×10^{-6}), the photon is assumed to be totally absorbed. The photon tracing process is repeated for all of the photons in the pre-specified number limit. In the end, the averaged Stokes vector of all the photons is the signal received by the lidar; note, the IAB is the I component in the Stokes vector.

As stated above, the phase function used in the simulator is truncated. In order to conserve the polarization properties of the particles, the ratio of the other elements of the phase matrix to the phase function is held constant using

$$P'_{ij}=\frac{P_{ij}}{P_{11}}P'_{11}, i,j=1,2,3,4 \tag{12}$$

where P_{ij} and P'_{ij} are original and truncated phase matrix elements, respectively.

Due to the phase function truncation, the output of the model is inconsistent with the specified cloud properties and needs correcting. The direct model output of IAB is

$$\gamma'_t=\frac{1}{2\eta_t S_t}\left(1-e^{-\eta_t\tau'}\right) \tag{13}$$

#253394 Received 5 Nov 2015; revised 21 Dec 2015; accepted 4 Jan 2016; published 8 Jan 2016
© 2016 OSA

where the subscript t indicates truncation and τ' is the scaled optical depth. According to Eq. (3) and the relation between P_{ij} and P'_{ij}

$$\gamma'_t = \frac{P_{11}(180^\circ)}{8\pi\eta_t} \cdot \frac{\tilde{\omega}}{1 - f_{fwd}\tilde{\omega}} \left[1 - \exp\left(-\eta_t (1 - f_{fwd}\tilde{\omega})\tau \right) \right] \tag{14}$$

where f_{fwd} is the fraction of truncated energy of forward scattering. Thus, the ratio of actual IAB to the simulated IAB should be

$$\frac{\gamma'}{\gamma'_t} = (1 - f_{fwd}\tilde{\omega}) \cdot \frac{1 - e^{-\eta\tau}}{1 - e^{-\eta_t (1 - f_{fwd}\tilde{\omega})\tau}} \cdot \frac{\eta_t}{\eta} \tag{15}$$

In Eq. (15), only η_t and η are not pre-defined in the simulation. By setting a large enough optical depth with a constant cloud extinction coefficient, IAB is nearly a constant $1/(2\eta_t S_t)$, and η_t can be determined when IAB and S_t are known. The multiple scattering coefficient η is an adjustable parameter varying with cloud particle number concentration. In the present simulations, η is set to be the least square fitted values from co-located observations. With the same optical depth, a denser cloud with a smaller η potentially has a higher possibility for light to be scattered multiple times. From this perspective, the truncation process decreases the density of cloud particles in the simulation because the cloud optical depth is reduced with unchanged physical depth. Thus η_t is always larger than η.

The mean amount of the time during which a photon remains in the cloud is proportional to the optical depth specified in the model. After truncation, optical depths used in the calculation in fact become smaller. Furthermore, when optically thicker clouds are used in the model, photons are scattered more times. Due to the randomness of the Monte Carlo method, this will result in larger relative errors than in a thinner cloud with the same number of photons. Thus, much calculation time can be saved and errors are reduced if the truncation process is applied.

2.3. Backscatter refinement of the ice crystal scattering model

In our simulation, a one-layer ice cloud is assumed with varied cloud properties. The ice crystal model is based on a database developed by Yang et al. [45] that includes the scattering, absorption, and polarization properties of 11 ice crystal habits, with three degrees of surface roughening, at a number of wavelengths between 0.2μm and 100μm. The habits used in the MODIS Collection 5 (C5) [46, 47] and Collection 6 (C6) [48] cloud optical property retrievals are both included in the simulations. The MODIS C5 model is a mixture of 6 habits with smooth surfaces and the percentages of the habits vary with particle size. In previous studies of remote sensing and cloud radiative effects [49–52], ice crystal models with rough surfaces have been shown to provide better consistency between polarimetric, lidar, and infrared observations than those with smooth surfaces. The MODIS C6 model assumes only one habit, namely a severely roughened 8-column aggregate, which has been demonstrated to have better spectral consistency in cloud optical thickness retrieval [49]. Furthermore, radiative transfer simulations show quite close fitting of theoretical polarized reflectivity values to the PARASOL counterparts if the severely roughened 8-column aggregate model model is used [25]. With the MODIS C6 model, the bulk ice cloud optical properties are derived by assuming a Gamma particle size distribution with an effective variance of 0.1.

The phase function of randomly oriented ice crystals with smooth surface in backscatter direction has been shown having a backscattering peak [53] due to corner reflection effect [54–56]. In fact, although rough surfaces diminish the intensity of backscattered light to some

#253394 Received 5 Nov 2015; revised 21 Dec 2015; accepted 4 Jan 2016; published 8 Jan 2016
© 2016 OSA

extent, there is still a peak in the backscattering direction. Rigorous numerical calculations using II-TM show backscattering peaks in the phase functions of both smooth and rough particles (Fig. 2).

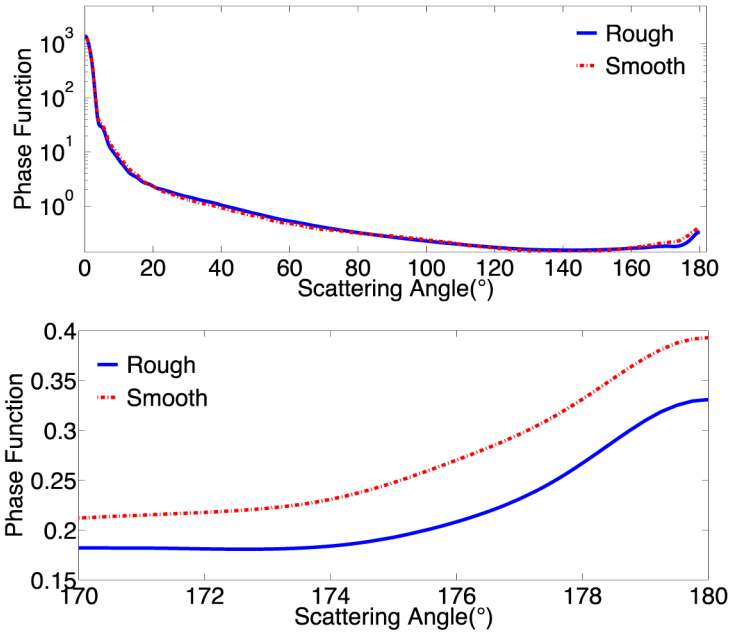

Fig. 2. Comparison between phase function of rough and smooth aggregate particles with size parameter 150 at 532 nm wavelength calculated by II-TM. Top: All scattering directions. Bottom: Backscattering directions

Nevertheless, when computational resources are limited, rigorous numerical simulations based on solving Maxwell's equations are only feasible in the small-to-moderate size parameter range (<150). The scattering properties of larger particles must be computed by IGOM, which is accurate for the phase function calculations except in a scattering range of 175°-180° where ignoring the interference of reflected light gives rise to substantial errors [32]. Zhou and Yang [32] proposed an empirical equation to modify the backscattering part of the phase function of a rough particle calculated by IGOM:

$$\zeta = \frac{P_m(\theta)}{P_{flat}} = 1 + \frac{\sin\delta}{\delta} R \tag{16}$$

where R is a constant and ζ is the ratio of the modified phase function (P_m) at backscattering angles (175°-180°) to a flat function derived from extrapolation of the phase function between 150° and 175°. Here, $\delta = 2\pi D(180^\circ - \theta)/\lambda$, where D is the maximum dimension of particle, θ is scattering angle ($175^\circ \le \theta \le 180^\circ$), λ is wavelength. For CALIPSO lidar simulations, Zhou and Yang [32] found that R = 0.7 is optimal to fit a previously retrieved lidar ratio 33 ± 5 *sr* [14] and multiple scattering coefficient 0.5-0.8 [57] for single hexagonal particles. However, the R value for severely roughened 8-column aggregates needs to be determined by rigorous numerical calculation. At the 180° scattering angle, Eq. (16) can be expressed as $\zeta = 1 + R$ for $\sin\delta/\delta \to 1$ when δ approaches zero, as given by L'Hôpital's rule [58]. Thus the R value can be acquired by comparing phase functions at 180° calculated by IGOM and II-TM in the size range where the II-TM is available.

#253394 Received 5 Nov 2015; revised 21 Dec 2015; accepted 4 Jan 2016; published 8 Jan 2016
© 2016 OSA

2.4. Satellite Data

In this study, the CALIPSO lidar Level-2 version 3 1km Cloud Layer product and the Collection 6 Aqua MODIS Level-2 cloud optical property product (MYD06) [59] are co-located to compare observed IAB and ICOD with simulations. The associated parameters include time, latitude and longitude from the two data sets, feature classification flags and the number of layers found from CALIPSO lidar product and cloud phase and cloud multilayer flags from MYD06. The geolocation and time parameters are used to find the pixels detected by lidar and MODIS at the same location simultaneously. Then the cloud phase and layer parameters are used to select pixels that are classified as single layer ice cloud with high confidence by the retrieval algorithms of the two data product.

The CALIPSO Cloud Layer product provides cloud top and base height as well as IAB at 532 nm and 1064 nm. MYD06 provides the cloud optical depth for the MODIS 660 nm spectral channel and effective particle radius. The effective particle radius in MYD06 helps select the ice cloud with effective radius from 20 microns to 60 microns. Spatial and temporal co-location of the two data sets thus provides IAB-ICOD relations for real ice clouds.

Since the MYD06 cloud optical depth retrievals correspond to the 660 nm spectral channel, it is therefore necessary to scale the data to 532 nm and 1064 nm for consistency with the CALIPSO lidar. The cloud optical depth at different wavelengths satisfies the relation

$$\frac{\tau_1}{\tau_2} = \frac{Q_{ext}\left(r_{eff}, \lambda_1\right)}{Q_{ext}\left(r_{eff}, \lambda_2\right)} \tag{17}$$

where Q_{ext} is bulk extinction coefficient. Therefore, the ice cloud optical depth at 650 nm can be scaled to the counterparts at 532 nm and 1064 nm using Eq. (17) by combining ice cloud particle effective radius retrievals with the bulk extinction coefficients of severely roughened 8-column aggregates. The bulk extinction coefficients are obtained from integration of particle size distribution and single particle extinction coefficients from Yang et al.'s database [45].

3. Results and Analysis

3.1. Backscatter Calculation

II-TM and IGOM are used to calculate the backscatter of severely roughened 8-column aggregate ice crystals. Figure 3 shows the comparison of the phase functions in the backscattering directions for aggregates with size parameter 130 at wavelengths 532 nm and 1064 nm.

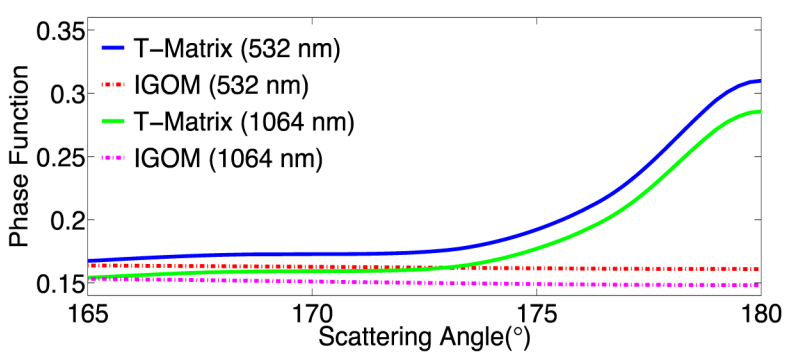

Fig. 3. Backscatter calculated by II-TM and IGOM of severely roughened 8-column aggregate with size parameter 130 at 532 nm and 1064 nm

#253394 Received 5 Nov 2015; revised 21 Dec 2015; accepted 4 Jan 2016; published 8 Jan 2016
© 2016 OSA

Obviously, the phase function calculated by II-TM has a strong backscattering peak compared with the counterpart produced by IGOM. II-TM rigorously solves Maxwell's equations and considers the interference and polarization states of electromagnetic waves involved in the scattering process. The effect may result in the enhancement of backscatter. In contrast, IGOM, based on the principles of geometric optics [31], is an approximate approach that is not able to accurately capture all relevant physical processes.

The dimensionless normalized backscatter values at the 180° scattering angle for various size parameters calculated by II-TM at two wavelengths are shown in Fig. 4. The integral of the normalized phase function over all solid angles is 4π.

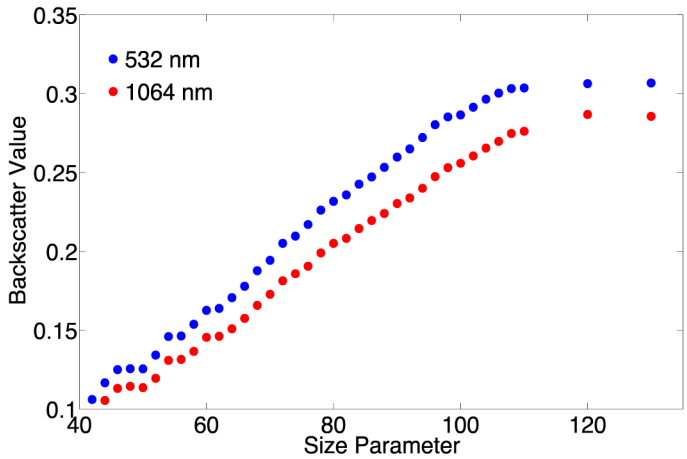

Fig. 4. Backscatter values calculated by II-TM versus size parameters at 532 nm and 1064 nm wavelength

For size parameters smaller than 100, the backscatter increases with increasing size parameter almost linearly. At size parameter around 100, it begins to approach an asymptotic value. The asymptotic values for the 532 nm and 1064 nm wavelengths are about 0.31 and 0.28, respectively. Due to limited computing resources, it is difficult to use the T-matrix method for larger size particles. However, from Fig. 4 it is reasonable to anticipate that the backscatter values for larger particles are nearly constant. This backscatter saturation phenomenon results from weakening of the diffraction effect in particle edges with increased size parameters. For larger size parameters, less light is diffracted by the edges of the particle and more light is reflected. When the edge diffraction approaches zero, the backscatter tends to be a constant. The asymptotic limit of backscatter may vary with different particle habits and surface roughness.

3.2. Backscatter Modification

The backscatter calculated by IGOM also reaches asymptotic values at the 532 nm (0.19) and 1064 nm (0.17) wavelengths at nearly the same size parameter. Therefore, the *R* values for backscatter enhancement at the two wavelengths are about 0.61 and 0.6, respectively.

An ice cloud with rough aggregate particles should have lidar ratios of 40.5 *sr* at 532 nm and 45.0 *sr* at 1064 nm, as calculated by Eq. (3). However, previous studies by Chen et al [17] and Josset et al [14] estimated the cirrus lidar ratio to be 29 ± 12 *sr* and 33 ± 5 *sr* at 532 nm, respectively. Thus the model with only rough aggregates may overestimate the lidar ratio of a realistic ice cloud. In other words, real ice clouds show somewhat stronger backscatter than that suggested by the rough aggregate model. Naturally, though ice crystals with rough surfaces may predominate an ice cloud, there are likely a small fraction of smooth ice crystals. Because smooth ice crystals have much stronger backscatter than rough crystals, it is

#253394 Received 5 Nov 2015; revised 21 Dec 2015; accepted 4 Jan 2016; published 8 Jan 2016
© 2016 OSA

plausible to expect that an ice cloud model with a mixture of rough and smooth particles be an optimal representation of a realistic ice cloud.

The optical properties of an ice cloud having both smooth and rough particles can be calculated by

$$X_{mix} = wt_s \cdot X_s + (1 - wt_s) \cdot X_r \tag{18}$$

where wt_s is a weighting parameter related to the fraction of smooth particles, and X is any optical parameter such as the phase matrix, SSA, or extinction coefficient, with subscript s indicating smooth particles and r indicating rough particles. The weighting parameter wt_s is a function of the fraction of the smooth particles and its mean extinction cross section, such that

$$wt_s = \frac{f_s C_{ext,s}}{f_s C_{ext,s} + (1 - f_s) C_{ext,r}} \tag{19}$$

where f_s is the fraction of smooth particles in the ice cloud in terms of number concentration, and $C_{ext,s}$ and $C_{ext,r}$ are, respectively, the mean extinction cross sections of smooth and rough particles.

Figure 5 shows a comparison of the phase functions of the modified MODIS C6 ice cloud model with (green line) and without (blue line) smooth particles, as well as the MODIS C5 model (dash-dot red line). The phase functions are plotted for the 532 nm (a,b) and 1064 nm (c,d) wavelengths with effective diameter 60 microns.

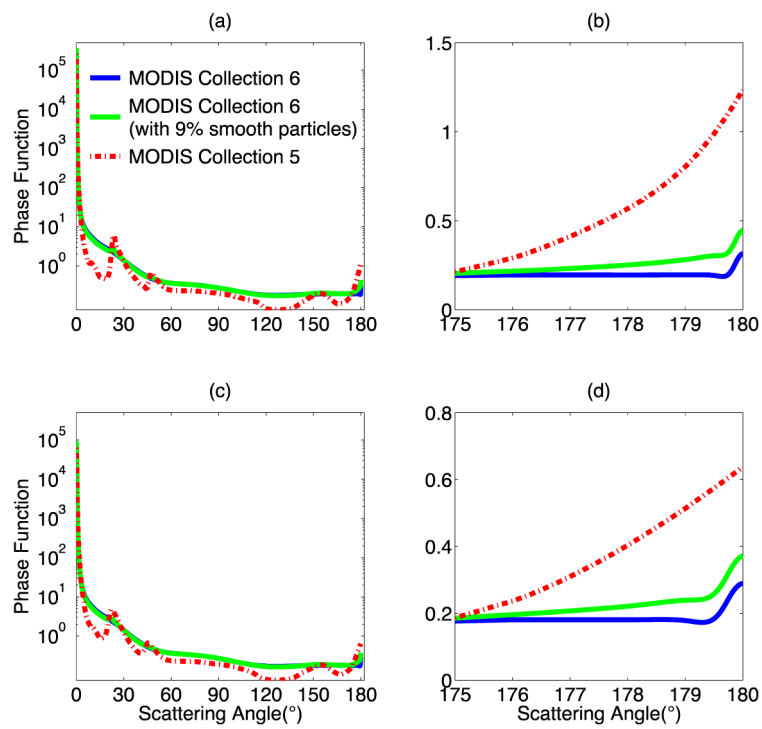

Fig. 5. Comparison of phase functions of modified MODIS C6 model without smooth particles (blue line), with 9% smooth particles (green line), and MODIS C5 model (dashed red line) at two wavelengths 532 nm (a, b) and 1064 nm (c, d) for effective diameter 60 microns. (a) and (c) show whole phase functions, and (b) and (d) show the backscattering parts.

#253394 Received 5 Nov 2015; revised 21 Dec 2015; accepted 4 Jan 2016; published 8 Jan 2016
© 2016 OSA

The halo peaks in the MODIS C5 phase function are not seen with the MODIS C6 model, as surface roughening acts to smooth the phase function. The lidar observations are very sensitive to the backscatter peak with the measured backscatter sensitive to differences in the LR. The LRs of the models of MODIS C5, modified MODIS C6 without and with 9% smooth particles are 10 *sr*, 40.5 *sr* and 32 *sr* at 532 nm and 20 *sr*, 45 *sr* and 34 *sr* at 1064 nm respectively.

3.3. Simulation Results and Comparison with Data

The IAB-ICOD relations of the three ice cloud models (i.e., smooth, rough, and a mixture of smooth of rough ice particles) introduced above are simulated. Forward modeling parameters, including optical depth, cloud top and base height, are obtained from co-located CALIPSO and MODIS data. The simulated IAB is compared with measured IAB at two wavelengths.

The co-located data ranges temporally from January 1st 2015 to February 1st 2015, and spatially over the Pacific and Atlantic oceans between 60°S and 60°N. The parameters including cloud top, cloud base height and ice cloud optical depth from a randomly selected 590-pixel co-located data subset are used in the simulation. Comparisons between the simulations and observations are shown in Fig. 6 and Fig. 7.

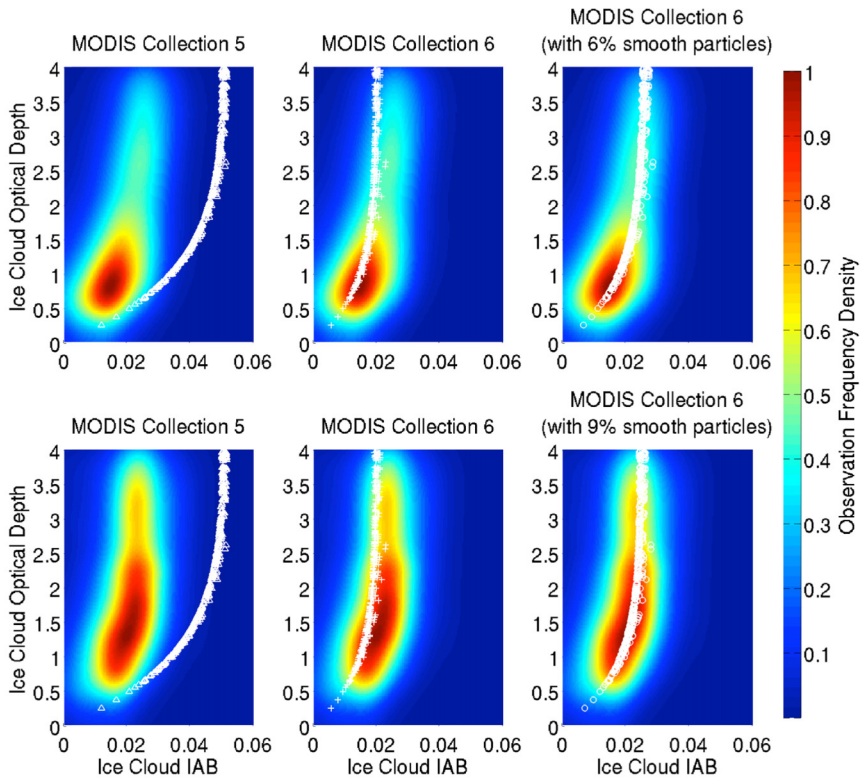

Fig. 6. Comparison of simulated IAB-ICOD relations and data in two latitude ranges at 532 nm wavelength. The simulated ice cloud has effective radius 30 microns and the observed ice cloud has effective radius from 20 microns to 60 microns. Top row: 30°N to 30°S. Bottom row: 30°N to 60°N and 30°S to 60°S.

Obviously, the simulation results using the MODIS C5 model (left columns in Figs. 6 and 7) deviate significantly from the measured IAB-ICOD relation. In contrast, the MODIS C6 model with only rough aggregates (middle columns) fits fairly well, but adding a small fraction of smooth particles (right columns) yields a better fit. The observations are shown for two latitude bands, namely the low latitudes (30°N to 30°S) the middle latitudes (30°N to

#253394 Received 5 Nov 2015; revised 21 Dec 2015; accepted 4 Jan 2016; published 8 Jan 2016
© 2016 OSA

60°N and 30°S to 60°S). The distribution of observation frequency in Fig. 6 suggests that in middle latitudes (bottom rows in Figs. 6 and 7) ice clouds are generally optically thicker than in low latitudes (top rows), which may reflect temperature differences. Applying least square fitting to the two groups of data, the best fitted lidar ratio S and multiple scattering coefficient η can be obtained by

$$\frac{\partial^2\left[\sum_i\left(\gamma_d'(\tau_i)-\gamma_r'(S,\eta,\tau_i)\right)^2\right]}{\partial S\partial\eta}=0 \tag{20}$$

where γ_d' is the IAB from CALIOP and γ_r' is calculated using Eq. (2) with all possible pairs of S and η. The best-fitted S and η at 532 nm for the IAB-ICOD relation in low latitudes are 35.57 *sr* and 0.58, respectively, and in middle latitudes are 32.28 *sr* and 0.65, respectively. The best fitted multiple scattering coefficients are used in Eq. (15) as η in the simulations. Associated backscatter values are around 0.35 for low latitudes and 0.39 for middle latitudes, which correspond to smooth particle fractions of roughly 6% and 9%, respectively.

The same analysis procedure is applied for IAB-ICOD relation at 1064 nm shown in Fig. 7.

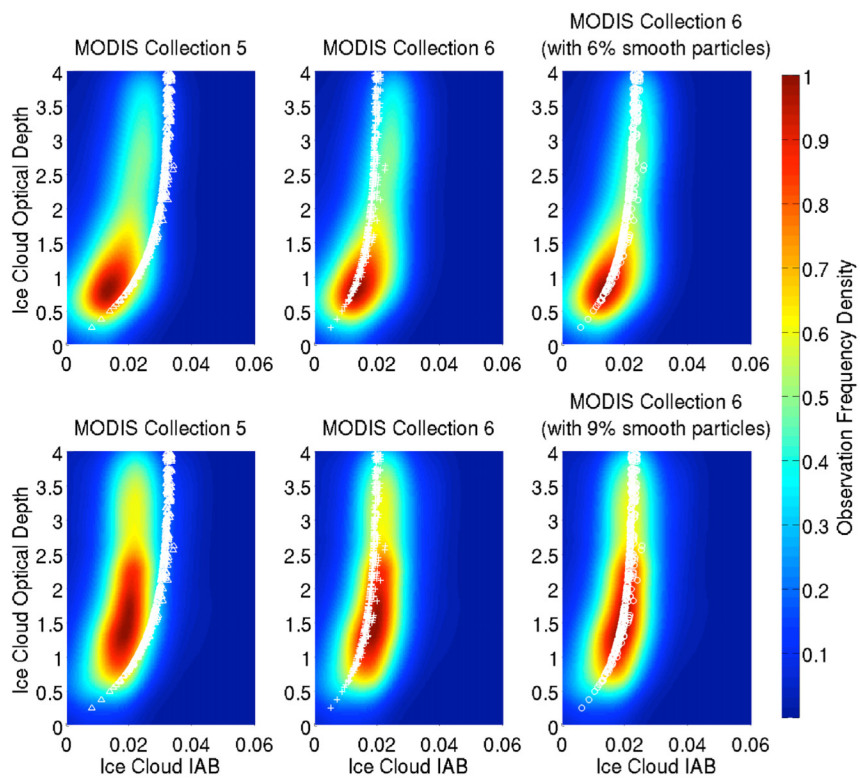

Fig. 7. Comparison of simulated IAB-ICOD relations and data in two latitude ranges at 1064 nm wavelength. The simulated ice cloud has effective radius 30 microns and the observed ice cloud has effective radius from 20 microns to 60 microns. Top row: 30°N to 30°S. Bottom row: 30°N to 60°N and 30°S to 60°S

The best fitted S and η values at 1064 nm are 37.5 *sr* and 0.58, respectively, in low latitudes, and 33.8 *sr* and 0.67, respectively, in middle latitudes. The fractions of smooth

#253394 Received 5 Nov 2015; revised 21 Dec 2015; accepted 4 Jan 2016; published 8 Jan 2016
© 2016 OSA

particles are also about 6% and 9%, which reveals the spectral consistency of the ice cloud model.

In summary, though the fraction of smooth particles may not be precise, the results suggest that there may be more smooth ice particles in ice clouds over middle latitude oceans than over low latitude oceans. This zonally non-uniform distribution of smooth particles may have multiple causes such as temperature differences [60–62]. As an indicator of cloud particle density, the ice cloud η at both wavelengths is smaller over low than middle latitudes, thus ice crystals may have a higher number concentration in low than in middle latitudes. It may also indicate that the cloud temperature is colder in the tropics. Since generally, colder clouds will have smaller ice crystal sizes and thus less energy scattered into the forward direction, which may indicate a larger multiple scattering coefficient.

4. Summary and Conclusion

This study focuses on the backscatter of ice clouds. The single-scattering properties of 8-column aggregate ice crystals are calculated by both numerically rigorous and approximate methods. A CALIPSO lidar simulator based on a Monte Carlo radiative transfer model is then used to simulate the integrated attenuated backscatter-to-cloud optical depth (IAB-ICOD) relation of the refined ice cloud model. The simulation results are compared with co-located MODIS and CALIPSO data, and provide rationale in support of the simulated backscatter. In addition, some characteristics of ice clouds, namely the fraction of smooth ice crystals, are inferred from backscatter information.

The invariant imbedding T-matrix method as a numerically rigorous method is used to calculate the phase function of 8-column aggregate ice crystals with size parameters smaller than 150. It is shown that there is a significant backscatter peak in the phase functions for both smooth and rough particles. The backscatter value increases linearly with size parameter, and reaches a constant at size parameter above 100. Therefore, though the T-matrix method is not feasible to calculate large particles, it is reasonable to assume that the backscatter of larger particles is nearly constant. IGOM does not compute a backscattering peak in the phase function that is calculated using II-TM. An empirical formula proven to be correct in backscatter simulation is applied to modify phase functions calculated by IGOM. The modified backscatter is consistent with the accurate value calculated by II-TM. Nevertheless, the corresponding lidar ratio is apparently too large compared with observed values that are typically around 30. One possible explanation is that real ice clouds contain a certain fraction of smooth particles that have enhanced backscattering.

To verify the modified ice cloud model, a CALIPSO lidar simulator is used to simulate the IAB-COD relation for the MODIS C5 ice cloud model and the backscatter–adjusted MODIS C6 counterparts with and without smooth particles. Furthermore, the simulation results are compared with co-located MODIS and CALIPSO data from two different latitudinal bands. The IAB-ICOD relation of MODIS C5 shows substantial deviations from the observations. For MODIS C6 adjusted with backscatter, the simulated IAB-ICOD relations fit the observed data reasonably. The quality of the fits is improved further when a small fraction of smooth particles are added. Fitting the simulated IAB-ICOD relations shows that, for the roughened ice crystal model assumed in the present study, the fractions of smooth particles in ice clouds over low and middle latitude oceans are, respectively, 6% and 9% with similar results at both CALIPSO wavelengths. This implies that ice clouds over middle latitude oceans may contain more smooth particles. In addition, the significant difference of multiple scattering coefficients in the two latitudinal bands may suggest a higher particle number concentration in lower latitudes and lower temperature for tropical ice cloud. Further quantitative research and in situ measurements are needed to confirm these findings about ice crystal habits, properties and distribution.

#253394 Received 5 Nov 2015; revised 21 Dec 2015; accepted 4 Jan 2016; published 8 Jan 2016
© 2016 OSA

Acknowledgments:

This study is supported by a NASA grant (NNX11AK37G) and a National Science Foundation (NSF) grant (AGS-1338440) and partially by the endowment funds (TAMU 512231-10000) related to the David Bullock Harris Chair in Geosciences at the College of Geosciences, Texas A&M University.

128.138.108.50 {ts '2018-02-26 12:46:05'}